Ocean Engineering 103 (2015) 223–236

Contents lists available at ScienceDirect

Ocean Engineering

journal homepage: www.elsevier.com/locate/oceaneng

Simulating and forecasting ocean wave energy in western Canada

Gordon Reikard [a,*], Bryson Robertson [b], Bradley Buckham [b], Jean-Raymond Bidlot [c], Clayton Hiles [d]

[a] U.S. Cellular®, Chicago, IL, United States
[b] University of Victoria, Victoria, BC, Canada
[c] European Center for Medium-range Weather Forecasts, Reading, UK
[d] Cascadia Coast Research, Ltd., Victoria, BC, Canada

ARTICLE INFO

Article history:
Received 22 July 2014
Accepted 30 April 2015

Keywords:
Ocean wave energy
Simulation
Forecasting
Physics models
Time series models

ABSTRACT

While the technology now exists to harvest wave energy in coastal regions, the capital expenditures for wave farms can be substantial, so it is important to be able to simulate the power in advance. Further, to integrate wave energy into the grid, utilities need to forecast over short horizons and calculate reserve requirements. Wave farms are simulated at three locations in British Columbia, Canada. Power series are calculated for six types of wave energy converters (WECs), four that operate in deep water, and two in shallow water. Forecasts are run using a physics-based model and statistical models. Five major conclusions emerge from the analysis. First, given the intermittency of buoy data, physics model hindcasts are an effective method of interpolating missing values. Second, the power output from converters does not have the same properties as the wave energy flux. Instead, the power output is a nonlinear function of the wave height and period, with fewer large outliers. Third, time series models predict well over near-term horizons while physics models forecast more accurately over longer horizons. The convergence point, at which the two types of models achieve comparable degrees of accuracy, is in the area of 2–3 h in these data sets, lower than in most prior studies. The recommendation is to use time series methods to forecast at the horizons required for reserves, and physics models for long-term planning. Fourth, the predictability of the power output can differ substantially for individual converters. Finally, wave energy is found to be significantly less costly in terms of reserves than wind and solar.

1. Introduction

While the technology exists to harvest wave energy, there are still several economic and technical barriers to widespread development of wave farms (Esteban and Leary, 2011; Arinaga and Cheung, 2012). The first and most obvious is identifying locations. British Columbia, on the Pacific coast of Canada, is favorably situated. Off the coast of Vancouver Island, the near-shore wave energy flux averages about 30 kW per meter of crest length (kW/m). Further from shore, the mean wave energy increases to 40 kW/m, and at the edge of the continental shelf, it is closer to 50 kW/m (Robertson et al., 2014).

A second issue is that capital expenditures can be substantial, so it is useful to be able to simulate the power output in advance. While some prior studies have used the standardized wave energy transport flux to estimate the power potential, matrices for various types of wave energy converters (WECs) have recently become available. This makes it possible to estimate the power output for particular devices. Simulated power series are calculated for six types of converters, four that operate in deep water, and two in shallow water.

A third issue is the intermittency of wave buoy data. In addition to missing hours or days, buoy records are often incomplete for weeks or months, due to equipment failure or other service issues. The proposed solution is to interpolate using retrospective simulations of a well-known physics-based wave model, SWAN (Simulating WAves Near shore).

A fourth issue is that the data at individual buoy sites is often volatile, with a great deal of random variation due to local sea conditions. Since wave farms are dispersed over wider areas, the noise should average out, making the power smoother and more predictable. Brekken et al. (2012) propose simulating wave parameters over large areas using the wave spectrum. The approach used here is to take weighted averages of nearby buoys. In this respect, the Vancouver data offers one crucial advantage: the buoys are close enough to create realistic simulations.

A final issue is forecasting. Short-term forecasting is used for operational planning, reserve usage, switching sources, and peak

* Corresponding author. Tel.: +1 773 399 8802.
E-mail address: Reikarsen@msn.com (G. Reikard).

http://dx.doi.org/10.1016/j.oceaneng.2015.04.081
0029-8018/

load matching. The relevant horizons can range from a few minutes to several hours. In forecasting wave energy, the analyst has a choice of two approaches, physics-based models or time series methods. Prior studies have found statistical models to be more accurate at short horizons, while physics models predict more accurately beyond the first few hours (Reikard et al., 2011). It is also possible to combine the two methods, for instance by ensemble averaging or using statistical models to correct the bias (Woodcock and Engel, 2005; Woodcock and Greenslade, 2006; Durrant et al., 2008; Pinson et al., 2012).

This study addresses all five issues. Buoy time series and physics model hindcasts are used to create data for the wave height and period, while WEC matrices are used to calculate power series. Section 2 sets out the databases. Physics model simulations are set out in Section 3. Section 4 deals with alternate measures of power and wave energy converters. The wave farm simulations are presented in Section 5. Section 6 compares the forecasting performance of time series and physics models. In Section 7, the cost of integrating wave energy into the grid is quantified using reserve calculations. Section 8 concludes.

2. The data

The databases were compiled as part of a broader research project by the Institute for Integrated Energy Systems at the University of Victoria. Table 1 reports the depth, time span, latitude and longitude for each of the buoys, along with the number of missing observations. Al the data sets include the significant wave height (H_{St}), in meters, and the mean wave period (T_{Mt}), in seconds, at an hourly resolution or better. Fig. 1 provides a map of the locations, and the bathymetry of the Vancouver coastline.

The Amphitrite Bank and Estevan Point buoys are located along the coast, at depths of 42–43 m, at a distance of 89 km from each other. The overlapping period for the two data sets is April 19, 2013 through January 27, 2014. The Amphitrite time series are more complete; the Estevan record is sparser. Further out on the continental shelf, there are two buoys at La Perouse bank, about 2 km from each other, at a depth of 74 m. The Environment Canada (EC) buoy provides a longer history, beginning November 23, 1988, and running through the present day. The second buoy, operated by the Coastal Data Information Program (CDIP), contains observations from April 30, 2012 through April 28, 2013. The data is at a 30 min resolution, but to make it compatible with the EC data, it was consolidated to 1 h. While the CDIP data set is much shorter, it is more complete for the overlapping period. The Florencia Bay site is at a depth of 25 m. The data consist of irregular observations, sometimes several records within the hour, while in other hours the values are missing completely. The database contains usable observations only for June 1, 2013 to January 27, 2014.

3. The Physics model simulations

Large-scale physics-based wave models have been in operation since the 1960s, and undergo continuous revision to improve performance (Hasselmann et al., 1976, 1980, 1985; Janssen, 1991, 2007). SWAN is a third generation phase-averaged Eulerian numerical wave model, designed to simulate the propagation of waves in shallow near-shore areas (Booij et al., 1999; Holthuijsen, 2007).

The wave action density (N) evolves as a function of time (t), distance in the Cartesian coordinates (x,y), the shifting of relative frequency due to variation in depths and currents (σ), and depth and current induced refraction (θ). Let C_g denote the wave action propagation speed in (x, y, σ, θ) space. Let S denote the combined source and sink terms. In deep water, the three major components of S are the input by wind (S_{IN}), nonlinear wave–wave interactions (S_{NL}) and wave dissipation through white-capping (S_{WC}). In shallow water, S includes the effects of bottom friction (S_{BF}) and shoaling-induced breaking (S_{BR}). The action balance equation can be expressed in the following form:

$$\partial N/\partial t + \partial C_{g,x}N/\partial x + \partial C_{g,y}N/\partial y + \partial C_{g,\sigma}N/\partial \sigma + \partial C_{g,\theta}N/\partial \theta = S/\sigma;$$

$$S = [(S_{IN}) + (S_{NL}) + (S_{WC}) + (S_{BF}) + (S_{BR})] \quad (1)$$

To develop the SWAN model simulations, a choice of ocean scale wind and wave inputs, and numerical wind wave growth/white capping solvers is required. The preferred boundary conditions for the SWAN model are directional wave buoy measurements. Unfortunately, appropriate directional measurements were not available for Vancouver Island. The best alternative is to use results from ocean-scale wind–wave models such as WAVEWATCH III (WW3). This study utilized publically available wave results from the Fleet Numerical Meteorology and Oceanography Center (FNMOC) ocean-scale operational WW3 model (Wittmann, 2001), and transient wind fields from the Coupled Ocean/Atmosphere Mesoscale Prediction System (COAMPS) wind model. An unstructured grid was used to provide both greater computational efficiency and improved resolution of nonlinear wave effects in shallower water. Within the area covered by the simulation, the depth ranges from approximately 1000 m at the continental shelf to 12 m just beyond the surf zone. In the deeper water, large grid spacing is sufficient, while in shallow water closer to shore the grid spacing must be much smaller, to capture the small scale wave transformations that occur due to interaction with the ocean floor. Grid spacing was specified proportional to water depth with a lower limit on spacing of 75 m. The proportionality constant was determined though a convergence analysis using the significant wave height (H_{St}) as a metric for convergence. The final SWAN model setup included Westhuysen's wind-growth/white capping formulation and SWAN frictional effects. For further documentation on optional set points, see SWAN (2006).

Table 1
The Vancouver buoy data.

Location	Depth (m)	Starting Date	Data End Date	Resolution	Latitude (N)	Longitude (W)	Missing values
Amphitrite Bank	43	4/19/2013	1/27/2014	Hourly	48.88	125.62	757
Estevan Point	42	4/23/2013	1/27/2014	Hourly	49.35	126.61	1682
Florencia Bay	25	5/31/2013	1/27/2014	Hourly	48.96	125.62	–
La Perouse Bank, Environment Canada buoy	74	11/23/1988	1/22/2014	Hourly	48.83	125.98	1421
La Perouse Bank, Coastal Data Information Program buoy	74	4/30/2012	4/28/2013	30 min	48.84	126.01	74

At all buoy sites, the data consist of the significant wave height and mean wave period.
At Florencia Bay, the observations are spaced irregularly for several months, with multiple values within an hour. The data is reasonably complete for the period from June 1 2013 through January 27, 2014. No data is available prior to May 31.

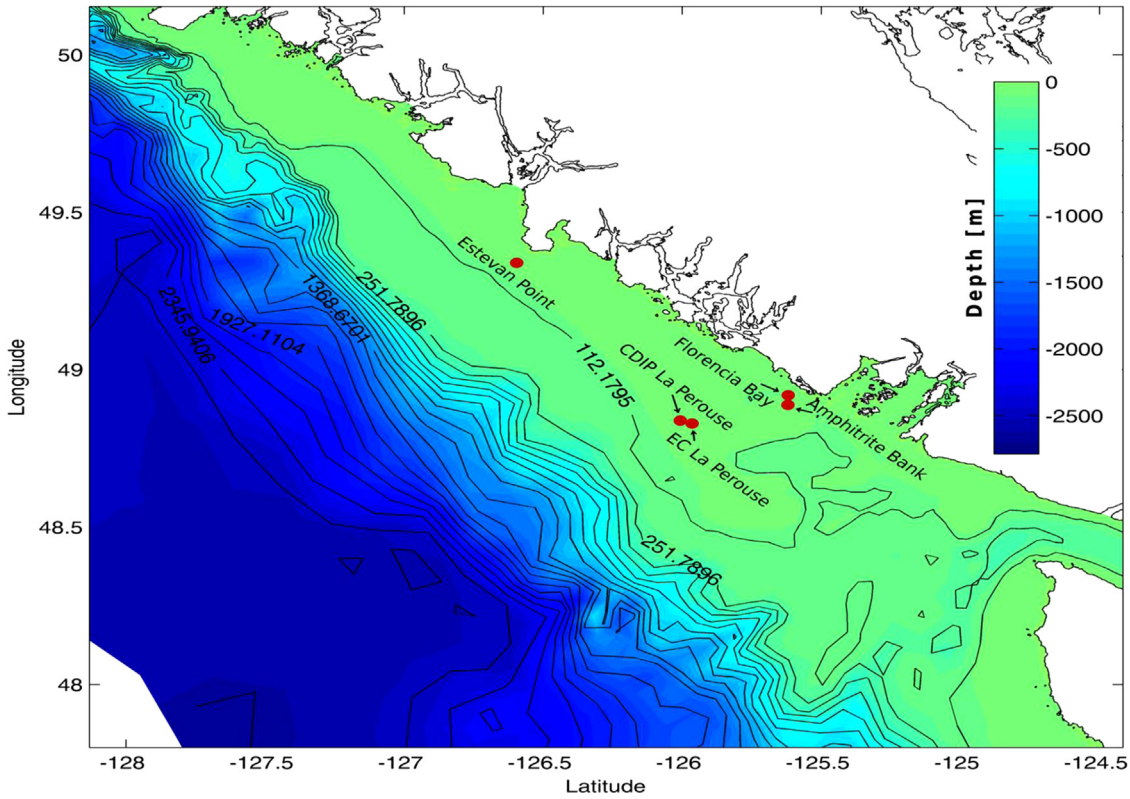

Fig. 1. The Buoy Locations and the Bathymetry of Vancouver Island. Source for bathymetry: Canadian Hydrographic Service.

The model was validated by comparing H_{St} and T_{Mt} from the SWAN hindcasts against the measured values at the buoy sites. Table 2 reports the bias (B), scatter index (SI), and correlation (r) for H_{St} and T_{Mt} at the EC, Estevan, Amphitrite and Florencia buoys. SWAN estimates H_S with a high degree of accuracy at all four locations. At La Perouse, the correlation is 0.95, and Amphitrite and Florencia, it is 0.92 while at Estevan it is only slightly lower, at 0.88. Similarly, the bias ranges from as little as −0.01 m at Amphitrite and Florencia to −0.04 at La Perouse and −0.06 at Estevan. The correlations are slightly lower for the wave period, but still quite good, 0.75 to 0.81. The wave period bias is less than 1 s on average.

After filling in the missing values with the SWAN hindcasts, the Amphitrite–Estevan database contains 6787 continuous observations. The La Perouse database runs from January 1, 2012 through April 28, 2013, providing 11,610 continuous observations (the CDIP values for January 1 through April 29 2012 are SWAN hindcasts). At Florencia bay, SWAN hindcasts were used for the first five months of 2013, as well as for the missing values over the next eight months. The final dataset consists of 9401 continuous observations, beginning January 1, 2013.

Table 2
Statistics comparing the buoy data and the SWAN simulations.

Variable	Buoy	Observation pairs	Bias (B)	Scatter index (SI)	Correlation (r)
H_S	La Perouse EC	8538	−0.04	0.18	0.95
	Amphitrite Bank	4092	−0.01	0.20	0.92
	Estevan Point	3379	−0.06	0.25	0.88
	Florencia Bay	3988	−0.01	0.18	0.92
T_M	La Perouse EC	8538	−0.86	0.18	0.81
	Amphitrite Bank	4092	−0.41	0.17	0.75
	Estevan Point	3379	−0.63	0.18	0.76
	Florencia Bay	3988	−0.61	0.19	0.66

The bias is denominated in meters for H_S and seconds for T_M. The modeled parameters are from the SWAN hindcasts. The measured values are from the buoys.

4. Wave power and converters

The next task is to convert the data into measures of power. The standard measure of wave power is the wave energy flux, E_{Ft}, denominated in kW/m. Let g denote the acceleration caused by gravity (9.8086 m/s/s), and ρ denote the density of seawater (1025 kg/m^3). For regular sea states in deep water, the flux can be defined according to the standard identity:

$$E_{Ft} = \left[(g^2\rho/64\pi)H_{St}^2 T_{Mt}\right] \approx 0.491\left(H_{St}^2 T_{Mt}\right) \quad (2)$$

To-date, any number of designs for WECs have been proposed, but no single technology has emerged as dominant. Parkinson et al. (2015) propose simulating a generic converter, in which the power is proportional to the flux for low values of the wave height. Since most converters have a maximum power rating, at higher values of the wave height the power level is assumed to be constant.

The approach used here however is to calculate power series using the matrices for several types of converters, as in Reikard (2013). There is a crucial difference between these approaches. In the flux, the energy is a function of the wave height squared. In the WEC matrices, the power output is a nonlinear function of the wave height and period, typically rising in proportion to the height, and then declining as the period increases. By implication, the power output from the matrices will be smoother than the flux.

Three generic types of WEC are used, surface attenuators, point absorber buoys, and oscillating converters. One device which has been in use for over a decade is the Pelamis, an attenuator designed to operate in deep water (Retzler, 2006; Henderson, 2006; Yemm et al., 2012; Pelamis, 2014). This converter consists of semi-submerged

Signficant Wave Height (meters)	Wave Period (seconds)																
	5.0	5.5	6.0	6.5	7.0	7.5	8.0	8.5	9.0	9.5	10.0	10.5	11.0	11.5	12.0	12.5	13.0
1.0		22	29	34	37	38	38	37	35	32	29	26	23	21			
1.5	32	50	65	76	83	86	86	83	78	72	65	59	53	47	42	37	33
2.0	57	88	115	136	148	153	152	147	138	127	116	104	93	83	74	66	59
2.5	89	138	180	212	231	238	238	230	216	199	181	163	146	130	115	103	92
3.0	129	198	260	305	332	340	332	315	292	266	240	219	210	188	167	149	132
3.5		270	354	415	438	440	424	404	377	362	326	292	260	230	215	203	180
4.0			462	502	540	546	530	499	475	429	384	366	339	301	267	237	213
4.5			544	635	642	648	628	590	562	528	473	432	382	356	338	300	266
5.0				739	726	731	707	687	670	607	557	521	472	417	369	348	328
5.5				750	750	750	750	750	737	667	658	586	530	496	446	395	355
6.0					750	750	750	750	750	750	711	633	619	558	512	470	415
6.5					750	750	750	750	750	750	750	743	658	621	579	512	481
7.0						750	750	750	750	750	750	750	750	676	613	584	525
7.5							750	750	750	750	750	750	750	750	686	622	593
8.0								750	750	750	750	750	750	750	750	690	625

Fig. 2. Conversion matrix for the Pelamis P2 device. Power is in kW.

cylindrical sections, moored perpendicular to the wave front. The segments move relative to one another as waves pass along the length of the machine. This wave-induced motion causes hydraulic cylinders to pump high pressure oil through hydraulic motors, which in turn drive generators. Electricity is transmitted along an umbilical cable to a junction on the sea bed. A single cable can be used for several devices. Fig. 2 shows the Pelamis power matrix. The machine attains its maximum power of 750 kW for a range of values of the height and period, generally 5.5 m or above, and 6.5–12 s. For the wave height, the resolution of the matrix was increased to 0.1 m, using linear interpolations.

Conversion matrices for three other types of WECs were calculated in Babarit et al., (2012). These matrices are reproduced in Appendices 1–3. The matrices were published at resolutions of 0.5 m and 1 s, but were increased to 0.1 m using the same procedure as for the Pelamis. Two of these converters are point absorbers, which use the rise and fall of waves to drive hydraulic pumps. The *floating two-body heaving converter* consists of a torus, which slides along a vertical spar. The power is generated by the relative motion of the two bodies. The maximum power for the design assumed here is in the range of 1000 kW. The *floating heave buoy array* is composed of several heaving buoys connected to a submerged reference structure via a hydraulic system. The number of buoys in this design was limited to ten, yielding a maximum power of slightly over 3600 kW.

A third type of WEC is an oscillating device, which typically has one end moored to the seabed, while the other end is free to move. Electricity is generated by the relative motion of the oscillating component. The *floating three-body oscillating flap device* consists of hinged flaps, which are connected to a common frame. The maximum power is 1665 kW.

Several converters have been designed for shallow locations. One of these, the *bottom-fixed heave buoy array,* has been deployed in Denmark, and is undergoing further development. The device consists of a jack-up structure, mounted on the seabed, with many floating buoys attached to fixed rocker arms. The conversion matrix is given in Fig. 3. The values up to wave heights of 3 m are from the Wavestar website (Wavestar, 2014), while values above this height are from Babarit et al. (2012). The power peaks in the area of 2200 kW.

The bottom-fixed oscillating flap device consists of pitching flaps oscillating around a fixed axis moored to the sea floor. Devices of this type are currently under development in Ireland and the United States. The device incorporates a pump located at a rotating shaft, which forces pressurized hydraulic oil or water to a shoreline station. On shore, the hydraulic energy is converted to electricity. The matrix is given in Appendix 4. The maximum power is in the area of 3300 kW.

5. The wave farm simulations

The first simulation combines data from the Amphitrite and Estevan buoys. The wave farm was assumed to consist of 101 installations, one each at Amphitrite and Estevan, and at 99 at points in between, roughly 0.9 km apart. The values for H_{St} and T_{Mt} were calculated using weighted averages of the two sites. The power output series were computed using the conversion matrices. Fig. 4 shows the flux, and Figs. 5 and 6 show the power series for the Pelamis and the heave buoy array, over a period of two months (November–December 2013). To facilitate comparison, the power is expressed as the average power per converter. Both the flux and the power output alternate between periods of high and low energy. The flux is more volatile, with intermittent large spikes. The power output is noticeably smoother, since the range of the outliers is limited by the WEC power ratings.

The second simulation uses the La Perouse data. Since the buoys are closer together, the wave farm was assumed to consist of 21 installations. Figs. 7–9 show the flux and the power series, over the period November–December 2012. Here too, the power output exhibits a rather different pattern from the flux. The flux shows irregular large outliers. The power output shows a tendency toward consistently high values but fewer extreme events.

The wave farm at Florencia relies more heavily on modeled values for the height and period. With only one buoy site, the WEC installations were simulated using SWAN hindcasts at five locations, running along a line parallel to the shore. The resulting values for H_{St} and T_{Mt} were converted to power output series for the bottom-fixed heave buoy array and oscillating flap devices. These were then scaled up to simulate 21 converters. Figs. 10–12 show the flux and the power output. There are fewer extreme outliers at this location, although there are several periods in which the energy alternates between low and intermediate states.

6. Forecasting experiments

The literature on using time series models to predict waves originates in the late 1990s. The methods include regressions and neural networks, although other methods such as genetic algorithms have been proposed (Deo and Naidu, 1998; Deo et al., 2001; Tsai et al., 2002; Deo and Jagdale, 2003; Ho and Yim, 2006; Londhe and Panchang, 2006; Jain and Deo, 2007; Tseng et al., 2007; Zamani et al., 2008; Roulston et al. 2005; Gaur and Deo, 2008).

The basic model used here is a regression on lags. Let Y_t denote a time series, *ln* denote natural logs, ω denote a coefficient, the subscript t denote time variation, and ε_t denote the residual:

$$\ln Y_t = \omega_{0t} + \omega_{1t} \ln Y_{t-1} + \omega_{2t} \ln Y_{t-2} + \omega_{3t} \ln Y_{t-3} + \varepsilon_t; \quad \varepsilon_t \sim P(0, \nu_t^2) \tag{3}$$

where P is the probability distribution and ν_t^2 is the residual variance. With hourly data, the Akaike (1973) criterion favored three lags. The coefficients are assumed stochastic. As demonstrated in prior studies, when the coefficients are time-varying,

Signficant Wave Height (meters)	Wave Period (seconds) 3	4	5	6	7	8	9	10	11	12	13	14	15	16
1.0		49	73	85	86	83	78	72	67	63	59	46	42	37
1.5	54	136	193	205	196	182	167	153	142	132	123	107	94	80
2.0	106	265	347	347	322	294	265	244	224	207	193	185	180	153
2.5	175	429	522	499	457	412	372	337	337	288	267	225	236	228
3.0	262	600	653	641	602	557	555	460	471	451	445	437	381	325
3.5				900	848	785	717	662	656	557	551	571	580	478
4.0				1123	1098	1030	984	825	857	821	830	735	635	652
4.5				1339	1339	1202	1181	1050	1140	1012	948	863	845	828
5.0				1689	1518	1403	1318	1248	1348	1115	1176	925	890	982
5.5					1943	1749	1517	1477	1374	1395	1376	1289	1212	1117
6.0					2192	2144	1618	1789	1586	1634	1783	1585	1346	1313

Fig. 3. Conversion matrix for the bottom-fixed heave buoy array. Power is in kW.

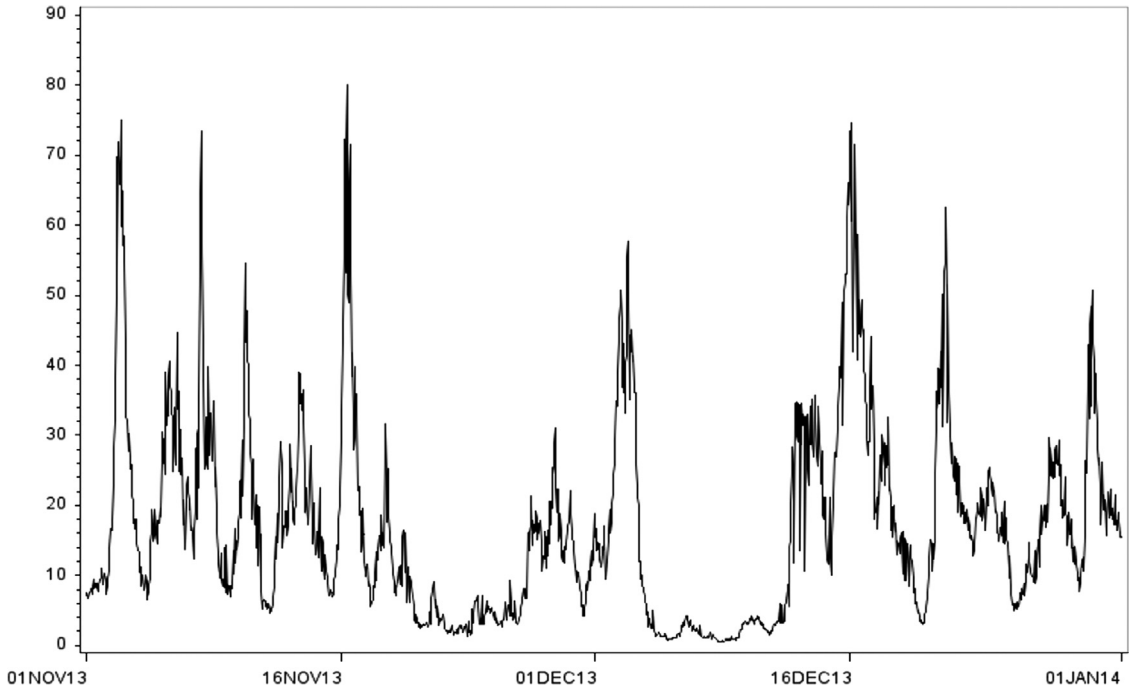

Fig. 4. Wave energy flux, Amphitrite-Estevan. Left scale: kW/m.

models of this type can capture a great deal of nonlinearity (Bunn, 2004; Granger, 2008).

It is also possible to forecast with physics-based models. The properties of physics model forecasts are quite different from those of statistical techniques. The errors have been found to decay only very slowly, over a period of several days (Bidlot et al., 2002). However, at short horizons, they can be less accurate, due to their dependence on local bathymetry, computational grid spacing and set-up boundary conditions. For recent evidence on model accuracy, see Garcia-Medina et al. (2013) and Chawla et al. (2012).

The forecasting experiments were run over four 15-day periods, July 1–15, October 1–15 and December 1–15, 2013, and January 1–15, 2014, using boundary spectra from the European Center for Medium-range Weather Forecasts (ECMWF) high resolution model. The wave model is fully interactive with the IFS Atmospheric model and provides hourly global output of wave spectra (Bidlot, 2012). The forecasts begin starting at zero and 12 h for each day, over a horizon of 48 h. In order to insure comparability, the time series models are run only for the same intervals as the SWAN forecasts.

Table 3 reports the findings for the Amphitrite–Estevan wave farm. At the 1 h horizon, the lowest forecast errors are achieved by the time series models: 22 percent for the flux, 19 percent for the Pelamis, 24 percent for the two-body heaving converter, 11 percent for the heave buoy array and 17 percent for the oscillating flap device. However, the accuracy of the time series models falls off very rapidly. Conversely, the SWAN error shows no visible trend. Instead, the SWAN error increases over the first few hours, but then oscillates. As with the statistical models, the accuracy of the SWAN forecasts also varies depending on the particular device. The points of convergence, at which SWAN forecasts more accurately than the time series models, are 3 h for the flux and most of the WECs, but as little as 2 h for the two-body heaving converter.

The La Perouse wave farm simulation extends only to April 2013, so a second database was created using the EC buoy and SWAN simulations. This data set runs from January to December 2013, so the accuracy calculations are for 2013 alone. Table 4 reports the forecast errors. Using the time series model, the errors are 18 percent for the flux and the Pelamis, 25 percent for the two-body heaving converter, 19 percent for the heave buoy array and 20 percent for the oscillating flap device. Here also, the SWAN error does not trend so much as fluctuate. The convergence point occurs at about 2 h for the flux, the oscillating flap device and the two-body heaving converter, and 3 h for the other two converters. At this location, SWAN effectively captures the transitions between periods of high and low energy, particularly in October and December. By comparison, the time series model imparts too much inertia to the forecast, missing the transition points.

For both locations, the two-body heaving converter consistently shows the highest forecast errors. The Pelamis device shows the

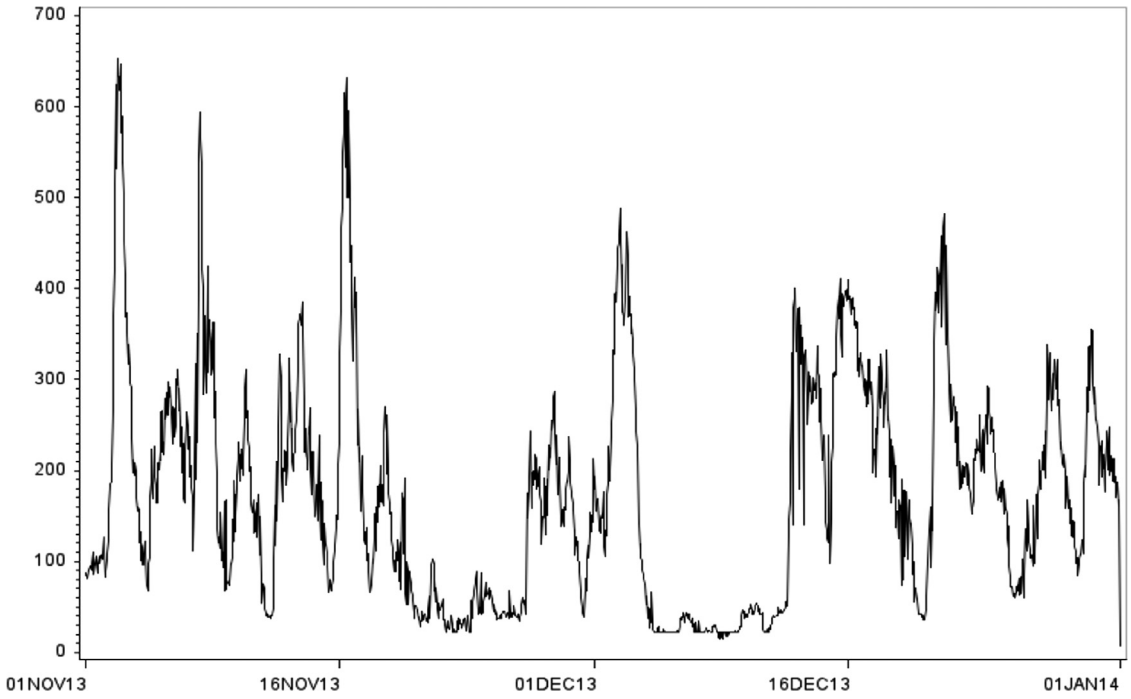

Fig. 5. Power output, Pelamis, Amphitrite-Estevan. Left scale: kW.

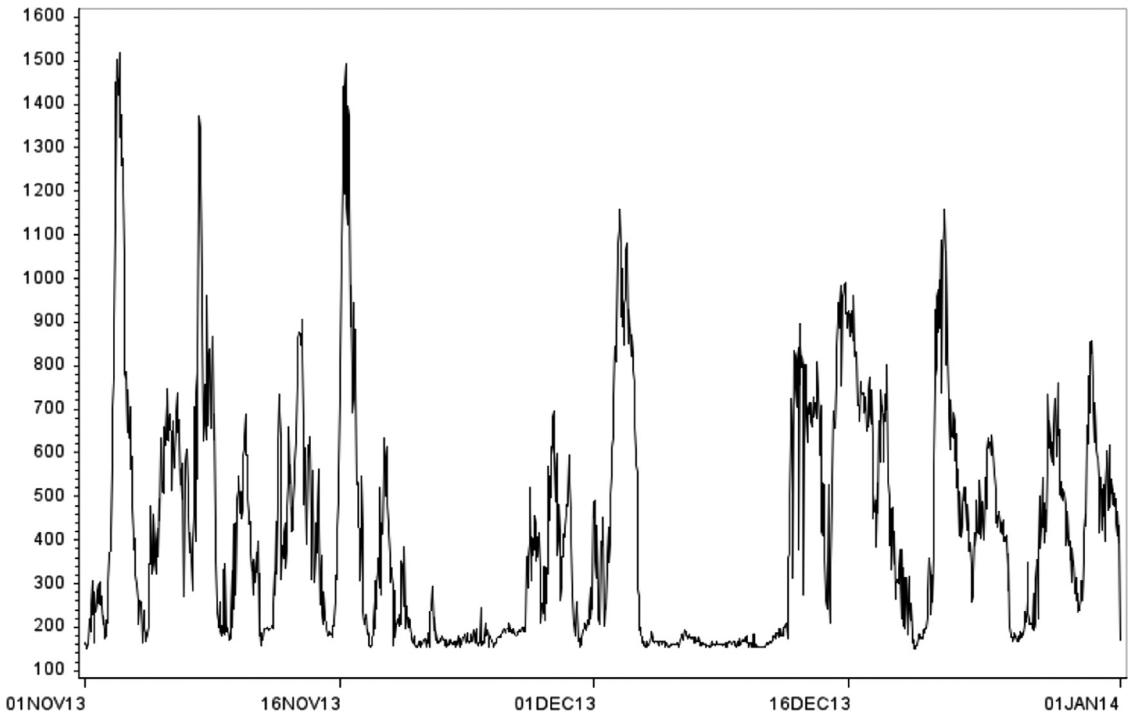

Fig. 6. Power output, heave buoy array, Amphitrite-Estevan. Left scale: kW.

lowest errors at the La Perouse site, while the heave buoy array performs best at Amphitrite–Estevan. Despite the greater depth, the forecast error is substantially lower at La Perouse than at Amphitrite–Estevan. Because of the greater wave heights at La Perouse, the Pelamis and two-body heaving converter frequently operate at their maximum power, a constant value. Conversely, at the Amphitrite–Estevan wave farm, both WECs consistently operate below their maximum power, so the resulting series are more variable.

Table 5 reports the findings for the Florencia wave farm. At the 1 h horizon, the time series model errors are 8.3 percent for the bottom-fixed heaving converter and 9.7 percent for the oscillating flap device. The accuracy deteriorates very rapidly, so that by 6 h the errors have surpassed 20 percent. By comparison, SWAN yields errors of 16 and 21 percent at the 1 h horizon, but the deterioration in accuracy is much slower. The convergence point for both converters is about 6 h. SWAN is a bit less accurate for the flux, where the convergence point is closer to 9 h. In contrast to the two deep water sites, the accuracy of the SWAN forecasts does deteriorate as the horizon increases. However, at long horizons, SWAN is substantially more accurate than the regression.

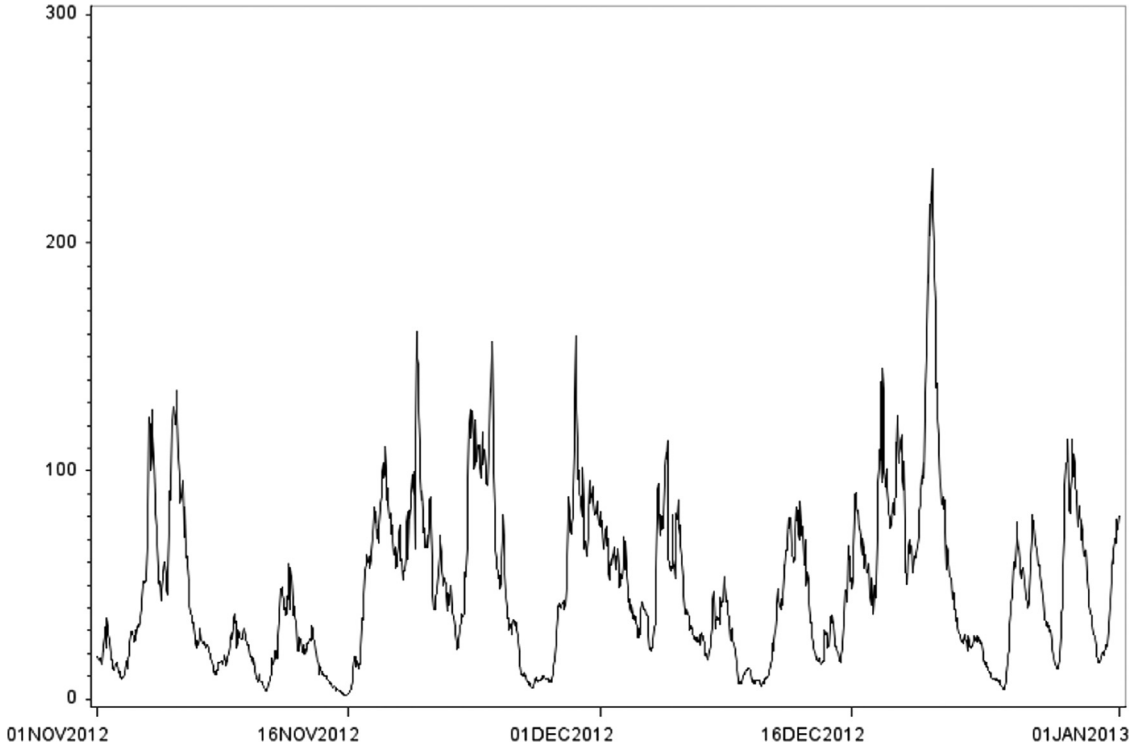

Fig. 7. Wave energy flux, La Perouse. Left scale: kW/m.

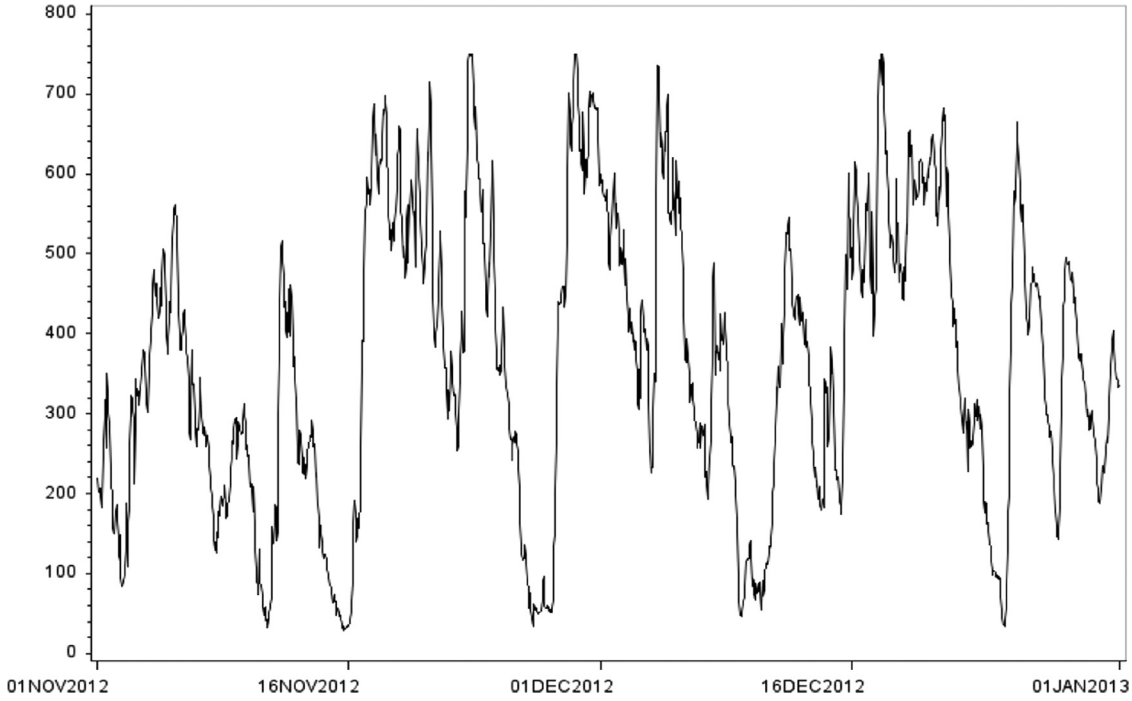

Fig. 8. Power output, Pelamis, La Perouse. Left scale: kW.

7. Integration into the grid

The final issue, and perhaps the most critical one for the power industry, is integrating wave energy into the grid. The cost of grid integration can be quantified in terms of reserves, i.e., generating capacity available to buffer against the uncertainty from variable energy sources. Load data is available from BC Hydro, the utility that serves British Columbia, from 2007 onward (BC Hydro, 2014). At BC Hydro, there are three categories of reserves. Regulating reserves are used to meet performance criteria on a minute-to-minute basis. Load following reserves are used to track changes in load over time horizons of 10 min. Balancing (or imbalance) reserves cover differences between the hourly load and the forecast 1 h ahead. Capacity-up reserves cover deficits in wave power relative to forecast, while capacity-down reserves cover wave power surpluses. Another interesting number is the net

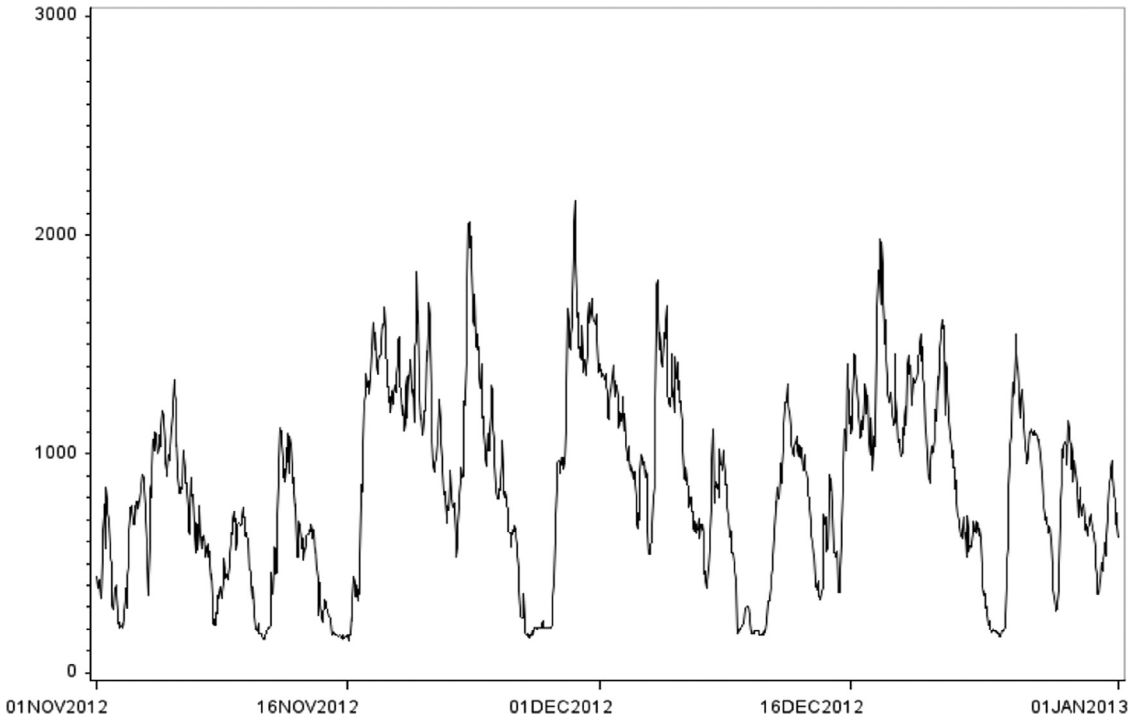

Fig. 9. Power output, heave buoy array, La Perouse. Left scale: kW.

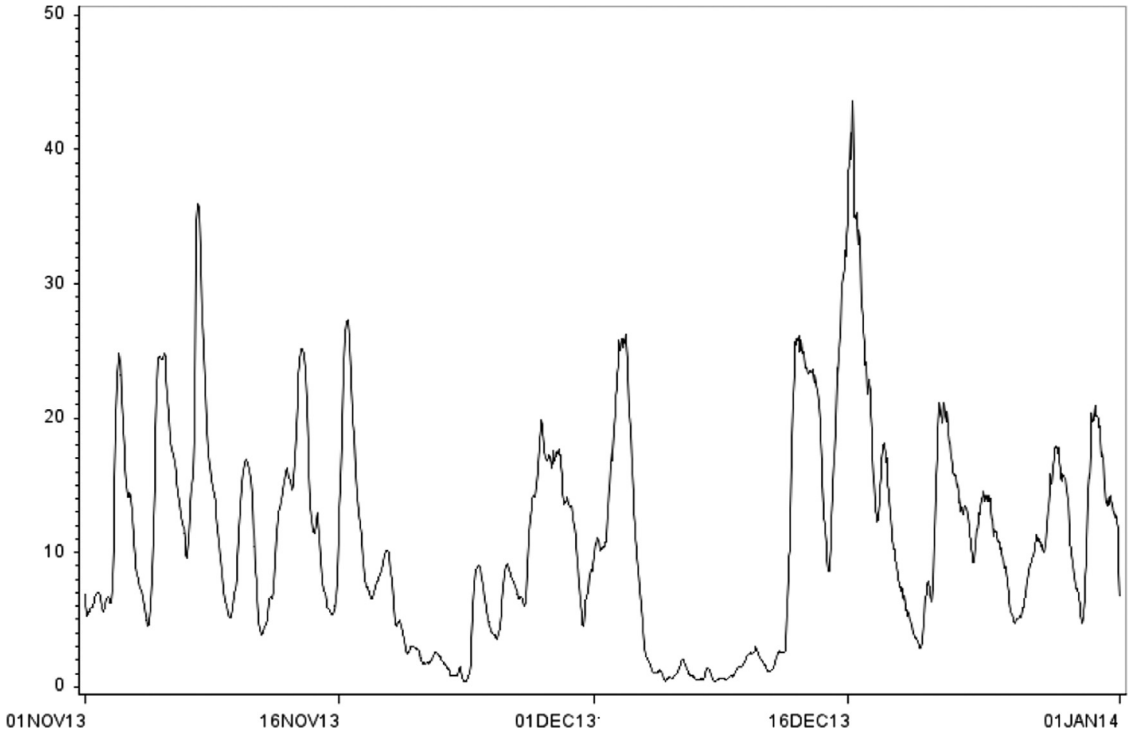

Fig. 10. Wave energy flux, Florencia. Left scale: kW/m.

power required from conventional sources, i.e., the load less the share supplied by wave power. Because of the nonlinear variability in waves, this is less predictable than the load itself.

The grid integration experiments were set up as follows. The first 500 observations were used as a training sample. The wave power output series were then forecasted iteratively, using the time series model, over a 1 h horizon. In each instance, the models were estimated over prior values, forecasted, then re-estimated over the most recent value, etc. All the predictions are true out-of-sample forecasts, in that they use only data prior to the start of the horizon. Time-varying parameter regressions can be estimated either using a Kalman filter (Kalman, 1960) or a moving window. With an unrestricted Kalman filter, the coefficients behave as a random walk, reducing predictive accuracy, so the moving window was used instead. Narrower widths allow high degrees of coefficient variation, while wider widths make the coefficients

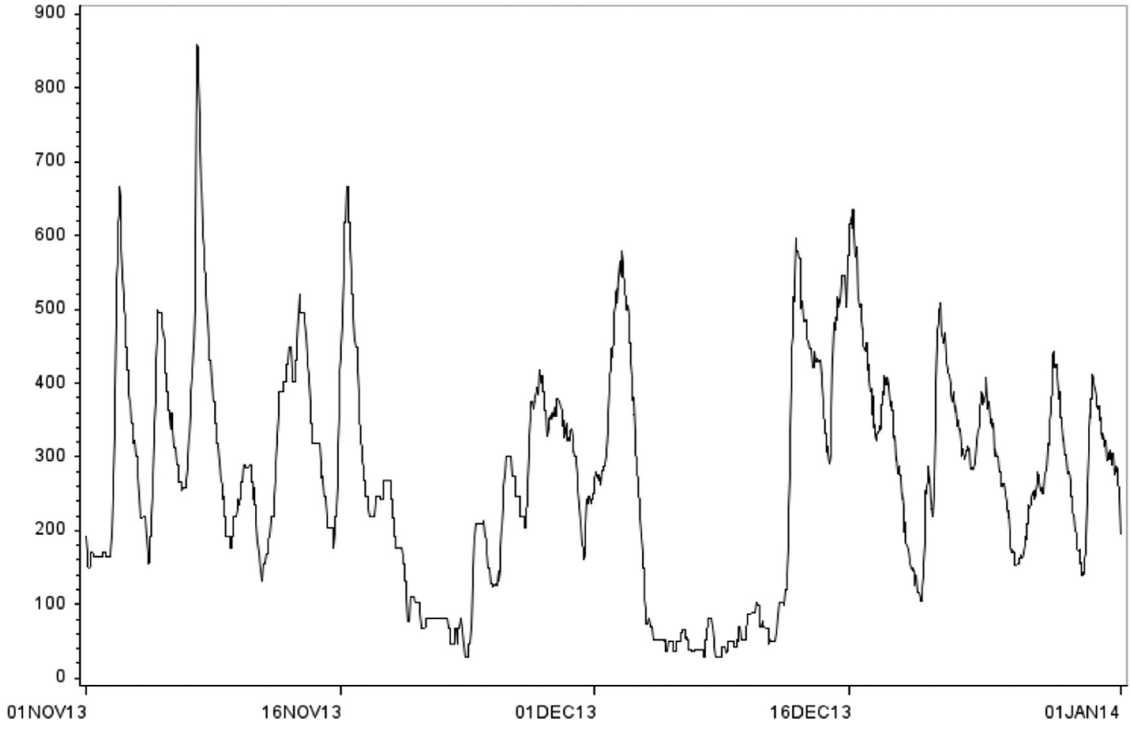

Fig. 11. Power output, bottom-fixed heave buoy array, Florencia. Left scale: kW.

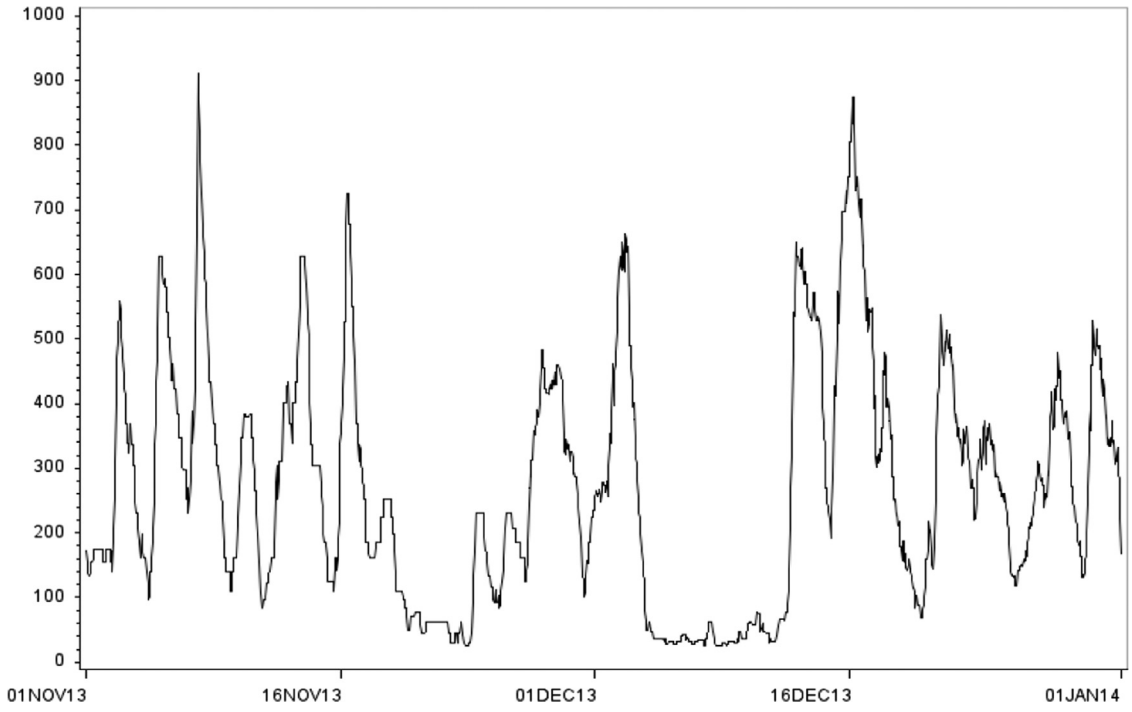

Fig. 12. Power output, bottom-fixed oscillating flap device, Florencia. Left scale: kW.

more inertial (Rossi and Inoue, 2012). The lowest predictive errors were found for widths in the range of 400–600 h. In the tests, a window width of 480 h was used.

To forecast the power load, the well-known ARIMA (autoregressive, integrated, moving average) class of models was used, again with time-varying parameters. Let Y_t denote the demand for power. Following the notation of Box and Jenkins (1976), let $\phi(L)$ be the autoregressive operator, represented as a polynomial in the backshift operator: $\phi(L)=1-\phi_1 L-\cdots-\phi_p L^p$, and $\Phi(L)$ be the seasonal autoregressive operator. Let $\theta(L)$ be the moving average operator: $\theta(L)=1+\theta_1 L+\cdots+\theta_q L^q$, and $\Theta(L)$ be the seasonal moving average operator. Let the superscript ξ denote the order of differencing, and the superscript ζ denote the order of seasonal differencing. Let the superscript f denote the cyclical frequency; for

Table 3
Forecast errors for Amphitrite–Estevan.

Forecast Horizon	Time series models					SWAN				
	Flux	Pelamis	Two body heaving converter	Heave buoy array	Oscillating flap device	Flux	Pelamis	Two body heaving converter	Heave buoy array	Oscillating flap device
1	22.60	19.47	24.13	10.58	17.41	33.65	38.15	41.38	21.10	31.65
2	34.67	27.62	37.84	16.36	21.19	41.98	33.64	26.75	22.60	23.71
3	45.80	35.69	47.10	22.50	25.75	34.73	30.95	26.75	17.45	20.54
4	58.40	39.36	62.74	20.08	34.74	39.98	37.75	37.00	15.94	32.75
5	54.42	41.79	60.48	21.53	33.07	36.37	29.69	27.75	17.13	20.62
6	75.41	52.65	87.26	25.56	48.82	40.19	34.69	32.86	17.88	29.03
7	91.66	53.68	100.16	29.27	51.22	41.52	31.95	29.85	14.31	26.66
8	84.37	52.97	92.00	26.82	48.07	43.90	35.88	38.77	18.76	28.95
9	88.43	55.26	99.83	29.59	49.91	57.66	43.59	45.04	32.06	35.96
10	99.16	62.31	111.28	29.57	56.15	49.36	36.16	36.22	19.49	30.40
20	88.79	63.45	92.60	41.22	54.22	26.89	23.54	29.42	17.71	22.15
30	134.97	81.86	112.36	40.97	61.74	46.68	30.11	42.84	26.78	26.14
40	129.73	80.66	111.42	35.33	63.67	59.42	45.26	44.85	44.74	27.88
48	153.27	93.67	128.42	35.52	77.55	41.60	29.21	33.10	18.27	24.02

Statistics are the mean absolute percent error.
Time period: selected dates in July, October and December 2013, and January 2014.

Table 4
Forecast errors for La Perouse.

Forecast Horizon	Time series models					SWAN				
	Flux	Pelamis	Two body heaving converter	Heave buoy array	Oscillating flap device	Flux	Pelamis	Two body heaving converter	Heave buoy array	Oscillating flap device
1	18.08	18.19	25.48	19.04	20.43	25.45	33.86	39.08	24.28	26.78
2	30.32	24.85	32.34	19.33	29.08	29.49	41.56	32.35	24.84	26.78
3	48.26	28.52	49.31	21.55	34.29	29.82	33.92	35.70	23.10	28.78
4	56.66	43.97	78.49	23.46	50.30	30.57	36.21	35.50	22.41	32.46
5	69.04	40.41	86.28	21.51	57.61	42.36	32.05	34.16	19.00	27.34
6	80.91	49.34	108.31	23.37	74.94	40.82	29.26	36.67	19.17	27.50
7	101.29	55.40	122.37	26.14	84.61	39.05	32.00	42.64	20.27	35.63
8	100.03	65.81	116.63	29.42	85.97	37.51	33.39	39.24	22.22	36.35
9	132.50	61.14	170.51	36.80	84.92	27.10	29.88	54.37	22.45	43.29
10	114.59	59.93	92.02	39.45	64.64	30.27	31.50	38.51	23.89	34.79
20	217.04	103.76	182.64	88.60	93.16	33.39	37.60	48.92	25.52	32.38
30	243.00	138.17	188.69	86.70	93.96	53.46	37.85	49.07	21.87	36.73
40	262.35	181.70	293.11	96.19	122.61	41.42	47.30	42.45	32.56	33.37
48	305.20	225.39	295.66	95.11	153.49	23.72	37.21	41.19	23.54	34.17

Statistics are the mean absolute percent error.
Time period: selected dates in July, October and December 2013.

the hourly data, $f=24$. The model is then of the form:

$$(1-L)^{\xi}(1-L^{f})^{\zeta}\ln Y_t=[\theta_t(L)\Theta_t(L)/\phi_t(L)\Phi_t(L)]\varepsilon_t \quad (4)$$

The hourly load forecasting model is an ARIMA (3,0,0)(2,1,0), i.e., three proximate lags, two lags at horizons of 24 and 48 h, and differencing at the 24 h horizon.

In order to be able to compare the reserves associated with different types of converters, the wave power was normalized to 500 MW, or 7.25 percent of the load. The forecasts are run for three time periods, coinciding with the intervals covered by the wave farm simulations. Table 6 reports the mean values for capacity-up and capacity-down reserves, expressed both in MW and as a share of the power. Table 7 reports the forecast errors for the load, the wave farms and the net power.

The errors for the aggregate load (Table 7) are fairly similar for all three periods, ranging from 0.76 to 0.89 percent. Balancing reserves (Table 6) are in the range of 53 to 59 MW, or less than 1 percent of the load. Capacity-up reserves are marginally higher than capacity-down reserves.

The forecast errors for the wave farms are lower than in the experiments for the shorter periods reported in Tables 3–5. These are the average errors for all points covered in the wave farm simulations.

Amphitrite–Estevan: At Amphitrite–Estevan, the wave power errors are 11.9 percent for the Pelamis, 14.4 percent for the two-body heaving converter, and 10–10.5 percent for the heave buoy array and oscillating flap device. The capacity-up reserves required for the Pelamis, the heave buoy array and the oscillating flap device range from 47 to 53 MW, or 7–10 percent of the wave power. The capacity-down reserves are range from −43 to −46 MW, or 8–11 percent of the wave power. The forecast error for the net power (Table 7) is in a narrow range of 1.41–1.45 percent. For the two-body heaving converter, reserves are higher 65 MW for capacity up and −64 MW for capacity down, or 13–14 percent of the wave power, while the net power error increases to 1.6 percent.

La Perouse: At La Perouse, the forecast errors are 7.8 percent for the Pelamis, 9.4 percent for the two-body heaving converter, 7.9 percent for the heave buoy array and 9.2 percent or the

Table 5
Forecast errors for Florencia.

	Time series models			SWAN		
Forecast Horizon	Flux	Bottom-fixed heaving converter	Oscillating flap device	Flux	Bottom-fixed heaving converter	Oscillating flap device
1	5.62	8.31	9.74	22.85	16.28	21.67
2	8.61	9.90	12.05	23.46	17.35	23.14
3	10.54	12.05	13.63	25.52	18.53	25.56
4	14.30	18.30	20.45	29.12	20.88	26.22
5	18.30	19.92	22.08	31.70	24.01	27.77
6	23.60	25.99	29.10	34.29	27.73	28.96
7	28.06	29.75	34.91	34.37	29.61	28.67
8	33.40	31.73	38.60	35.66	32.11	28.49
9	39.10	32.45	35.66	37.64	34.97	31.23
10	44.41	33.03	44.63	39.26	30.96	33.33
20	81.13	55.76	84.14	59.17	56.19	56.00
30	181.38	86.39	145.82	90.47	78.44	80.83
40	276.93	129.02	229.50	184.84	128.30	103.81
48	277.97	144.14	249.93	188.40	130.40	139.26

Statistics are the mean absolute percent error.
Time period: selected dates in July, October and December 2013.

Table 6
Balancing reserves.

	Hourly power scheduling			
Site and converter	Capacity up Reserves (MW)	Reserves/ power	Capacity down Reserves (MW)	Reserves/ power
Amphitrite–Estevan (500 MW)				
Aggregate Load	59.41	0.9	−58.06	0.9
Pelamis simulation	53.16	10.7	−45.65	11.6
Two-body heaving converter	65.26	12.6	−64.07	14.2
Floating heave buoy array	46.83	7.4	−42.81	7.9
Three-body oscillating flap device	48.54	9.7	−45.56	10.9
La Perouse (500 MW)				
Aggregate Load	52.98	0.8	−52.63	0.8
Pelamis simulation	27.49	6.3	−22.84	7.5
Two-body heaving converter	39.15	7.8	−32.59	9.1
Floating heave buoy array	31.21	5.7	−23.99	5.6
Three-body oscillating flap device	33.91	6.3	−27.91	6.8
Florencia (500 MW)				
Aggregate Load	57.68	0.8	−56.55	0.8
Bottom-fixed heave buoy array	22.42	4.4	−19.43	4.9
Bottom-fixed oscillating flap device	50.19	15.9	−47.57	13.5

The period covered by the Amphitrite–Estevan simulation is April 19, 2013 to January 17, 2014. The period covered by the La Perouse simulation is January 1, 2012 to April 28, 2013. The period covered by the Florencia simulation is January 1, 2013 to January 17, 2014. Statistics are the mean absolute value of reserves, and the mean ratio of reserves to power, expressed as a percentage.

oscillating flap device. The capacity-up reserves required for the Pelamis, the oscillating flap device and the heave buoy array are in the range of 27–33 MW, or 5.7–6.3 percent of the wave power. Capacity down reserves are even lower, −23 to −28 MW, or 5.6–7.5 percent of the power. The reserves for the two-body heaving converter are again higher. Capacity up reserves are 39 MW, or

Table 7
Forecast errors for the load and net power.

	Amphitrite–Estevan	La Perouse
Aggregate load	0.89	0.76
Pelamis	11.92	7.84
Two-body heaving converter	14.39	9.43
Floating heave buoy array	10.07	7.93
Three-body oscillating flap device	10.42	9.23
Net Power, Pelamis (load less Pelamis)	1.42	0.97
Net power, two body heaving converter	1.63	1.16
Net power, heave buoy array	1.45	1.08
Net power, three body oscillating flap device	1.41	1.12
	Florencia	
Aggregate Load	0.84	
Bottom-fixed heaving converter	4.64	
Bottom-fixed oscillating flap device	6.52	
Net power, bottom-fixed heave buoy array	1.03	
Net power, bottom-fixed oscillating flap device	1.15	

Statistics are the mean absolute percent error. The period covered by the Amphitrite–Estevan simulation is April 19, 2013 to January 17, 2014.
The period covered by the La Perouse simulation is January 1, 2012 to April 28, 2013.
The period covered by the Florencia simulation is January 1, 2013 to January 17, 2014.

8 percent of the power, while capacity down reserves are −32.6 MW, or 9 percent of the power. The net power error ranges from less than 1 percent for the Pelamis to 1.16 percent for the two body heaving converter.

Florencia: At Florencia, the forecast errors are 4.6.percent for the bottom-fixed heaving converter and 6.5 percent for the oscillating flap device. The capacity-up reserves are as little as 22.4 MW or 4.4 percent of the wave power for the bottom-fixed heave buoy array. Capacity down reserves are roughly −20 MW, or 4.9 percent of the power. The reserves are much higher for the oscillating flap device. Capacity up reserves are 50 MW, or 15.9 percent of the power, while capacity down reserves are −47.6 MW, or 13.5 percent of the power. The error for the net power is 1.03 percent for the heave buoy array and 1.15 percent for the oscillating flap device.

In order to provide some context for these reserve and error values, it is useful to compare them with calculations for wind and solar energy. Forecasting experiments for wind speed at the 1 h horizon have found that the minimum error, even in optimal wind conditions, is in the range of 12–16 percent, but more typically lies in a range of 25–30 percent (Reikard, 2008, 2010). For solar energy, the errors are usually higher. Forecasting tests for solar irradiance at ground level have found errors in the range of 20 percent in areas with little cloud cover, but errors closer to 40 percent in areas where cloud cover is heavier (Reikard, 2009).

BC Hydro does not release data on wind and solar power. However, wind and wind forecast time series have been published by the Bonneville Power Administration (BPA) in the United Sates. The BPA serves the region just south of British Columbia–Washington, Oregon, Idaho and parts of the surrounding states—so that its data sets provide a reasonable benchmark for comparison. Hourly values for reserves and wind power were downloaded for January 1, 2012 through December 31, 2013 (Bonneville Power Administration, 2014). BPA operates more than 40 wind farms, with a combined capacity of 4515 MW; the average hourly power was 1218 MW. Using BPA's hourly forecast for wind power, the mean error was 59 percent, although this is upwardly biased by a small number of extreme errors. If these are excluded, the error is in the 30 percent range. Capacity up reserves averaged 164 MW, or 16 percent of the wind power, while capacity down reserves averaged 115 MW, or 35 percent of wind power. These values are

of course not independent of scale. If they are scaled down to 500 MW, as in the wave simulations, the corresponding values would be 68 MW and 47 MW. These are still much larger, both in absolute terms and as a percent of renewable energy, than the values calculated for any of the wave farms.

8. Conclusions

This study has yielded several findings. First, physics model simulations are an effective way to interpolate missing values, particularly when dealing with extended gaps in the wave buoy records. One of their main strengths is their ability to capture seasonality. It is acknowledged that physics models hindcasts are smoother than buoy data. However, over the larger geographic areas spanned by wave farms, physics models may be more effective. The degree of smoothing implied by geographic dispersal can be substantial. At the sites analyzed here, the forecast errors for the wave farm power series are on the order of 30 percent lower than for the individual buoys.

Second, the power output from WECs does not have the same properties as the flux. The flux is by construction extremely volatile. The WEC power output exhibits much less variability. Both the flux and the power output exhibit seasonality, increasing during the autumn and winter months. However, during winter storms, when the flux can be very difficult to forecast, the power output can actually become more predictable as the converters reach their maximum ratings.

Third, time series models predict more accurately over short horizons while physics models are found to forecast more accurately over longer horizons. The convergence points range from 2 to 3 h at the deep water sites to 6 h at the one shallow site. This is lower than in previous studies. Despite this, at the 1 h horizon necessary for calculating reserves, the time series models are more accurate. The most likely explanation is that the physics model is capturing the underlying causal mechanisms at lower frequencies, while the time series model is picking up mainly on serial correlation (dependence between proximate time points) in the data. The recommendation is therefore to use time series models for short-term forecasts at the horizons required for reserves, but to use physics models for longer-term planning.

Fourth, the degree of forecast accuracy differs both for the particular WEC and the location. For the shallow water devices, the heave buoy array shows a much greater degree of accuracy than the oscillating flap device. For the deep water devices, the errors for the Pelamis, the heave buoy array and the oscillating flap device are in the same range at one site (Amphitrite–Estevan), while the error for the two body heaving converter are higher. At the other location, the errors for the heaving converter and oscillating flap device are higher than for the other two converters. The errors can also vary over particular intervals. For the longer periods spanned by the simulations, the average errors are lower than over the shorter intervals used in the SWAN-time series comparison. Further analysis is warranted, but the findings here indicate that attenuators and heave buoy arrays are less costly in terms of reserves.

Finally, integration of wave power into the grid requires lower reserves than wind and solar. The forecast errors at 1 h can be as low as 5 percent in shallow water. Based on the locations here, they are typically in the range of 10–14 percent at slightly deeper areas along coastlines and 8–10 percent in deep water. These are lower than for other types of renewable energy. In this sense, the findings argue in favor of developing wave power along the Pacific coast, and at sites with comparable conditions around the world.

Appendix A

Tables A1–A4.

Table A1
Conversion matrix for the floating two-body heaving converter. Power is in kW.

Signficant wave height (m)	Wave period (s)												
	4	5	6	7	8	9	10	11	12	13	14	15	16
1.0	6	11	19	25	30	44	50	53	44	34	22	20	17
1.5	13	25	43	55	68	90	102	92	91	66	65	45	37
2.0	24	45	65	100	121	153	175	151	122	126	87	61	58
2.5		65	104	141	191	179	243	255	190	181	135	99	83
3.0		96	137	205	244	357	293	353	260	248	184	137	120
3.5			192	254	291	431	385	424	314	285	239	222	172
4.0			256	366	403	551	536	531	473	420	289	268	179
4.5			327	418	574	678	708	665	509	415	386	244	240
5.0			358	514	658	824	828	618	638	512	452	384	333
5.5				610	774	880	936	905	805	603	456	397	311
6.0				711	952	974	1000	838	886	648	501	503	396
6.5				788	1000	1000	1000	1000	1000	727	577	435	424
7.0				781	1000	1000	1000	1000	1000	959	748	574	472

Table A2
Conversion matrix for the floating heave buoy array. Power is in kW.

Signficant wave height (m)	Wave period (s)												
	4	5	6	7	8	9	10	11	12	13	14	15	16
1.0	180	166	153	171	125	87	72	65	85	85	37	29	16
1.5	223	195	157	148	261	192	223	139	155	155	74	67	46
2.0			214	227	396	335	237	235	172	138	115	105	70
2.5				440	598	514	379	342	204	169	142	128	95
3.0				681	801	735	594	486	199	174	151	134	121
3.5				904	1035	949	788	617	239	209	183	164	146
4.0				1131	1269	1163	982	743	285	248	216	195	175
4.5				1358	1488	1374	1187	869	330	287	250	225	201
5.0				1585	1712	1585	1392	988	380	334	285	263	226
5.5				1812	1937	1798	2138	1107	429	381	323	301	261
6.0				2040	2162	2010	2884	1234	439	416	361	336	295
6.5				2267	2386	2221	3143	1360	449	450	406	372	329
7.0				2494	2611	2433	3619	1483	506	464	451	408	363

Table A3
Conversion matrix for the floating three-body oscillating flap device. Power is in kW.

Signficant wave height (m)	Wave period (s)												
	4	5	6	7	8	9	10	11	12	13	14	15	16
1.0	19	29	47	57	52	37	29	20	17	13	9	7	7
1.5	42	63	92	111	109	65	56	38	29	22	19	13	11
2.0	66	99	151	201	165	105	85	59	52	41	29	24	19
2.5		160	242	262	226	166	118	83	70	57	39	39	26
3.0		213	319	372	327	211	152	116	94	75	66	45	42
3.5			436	503	408	293	203	148	115	93	75	58	44
4.0			554	540	521	355	261	192	144	123	84	81	56
4.5			645	746	587	379	302	236	190	154	106	90	74
5.0			796	926	695	486	341	287	211	168	136	111	94
5.5				955	808	603	430	343	231	201	150	120	97
6.0				1161	957	642	481	329	289	212	172	146	111
6.5				1476	1039	702	488	397	312	237	204	153	120
7.0				1665	1197	821	612	466	385	252	223	181	146

Table A4
Conversion matrix for the bottom-fixed oscillating flap device. Power is in kW.

Signficant wave height (m)	Wave period (s)													
	3	4	5	6	7	8	9	10	11	12	13	14	15	16
1.0	25	27	39	57	76	87	104	109	100	101	98	94	94	87
1.5	61	63	92	126	168	201	213	201	239	207	198	183	150	154
2.0	71	75	160	233	301	380	408	383	399	329	365	319	265	259
2.5		250	254	378	467	568	623	616	601	519	523	481	390	428
3.0		360	368	503	693	799	824	876	792	759	704	546	579	554
3.5			650	655	934	1032	1085	1241	1075	973	925	862	747	688
4.0			840	843	1093	1352	1427	1430	1390	1158	1224	1139	1138	863
4.5				1219	1408	1644	1677	1807	1641	1662	1562	1404	1370	1191
5.0				1247	1670	1965	1962	2097	2002	1833	1798	1814	1479	1442
5.5					1979	2339	2308	2115	2389	2120	2012	1940	1518	1587
6.0					2406	2713	2776	2344	2705	2451	2396	2182	2414	2333
6.5					2778	3044	3001	2989	3211	3286	2896	2716	2455	2309
7.0					2871	3119	3131	3127	3176	3332	2877	2935	2676	2658

Appendix B. Supporting information

Supplementary data associated with this article can be found in the online version at http://dx.doi.org/10.1016/j.oceaneng.2015.04.081.

References

Akaike, H., 1973. Information theory and the extension of the maximum likelihood principle. In: Petrov, B.N., Csaki, F., Second International Symposium on Information Theory, Budapest, Akademiai Kiado, pp. 267–281.

Arinaga, R.A., Cheung, K.F., 2012. Atlas of global wave energy from 10 years of reanalysis and hindcast data. Renewable Energy 39, 49–64.
Babarit, A., Hals, J., Muliawan, M.J., Kurniawan, A., Moan, T., Krokstad, J., 2012. Numerical benchmarking study of a selection of wave energy converters. Renewable Energy 41, 44–63.
BC Hydro, 2014. http://transmission.bchydro.com/transmission_system/balancing_authority_load_data/historical_transmission_data.htm.
Bidlot J-R., 2012: Present status of wave forecasting at ECMWF. In: Proceeding from the ECMWF Workshop on Ocean Waves. ECMWF, Reading, United Kingdom, June 25–27, 2012.
Bidlot, J-R., Holmes, D.J., Wittmann, P.A., Lalbeharry, R., Chen, H.S., 2002. Intercomparison of the performance of operational ocean wave forecasting systems with buoy data. Weather Forecasting 17, 287–310.
Bonneville Power Administration, 2014. Website: www.bpa.gov. Wind and load data are available at: ⟨http://transmission.bpa.gov/Business/Operations/Wind/⟩.
Booij, N., Ris, R.C., Holdthuijsen, L.H., 1999. A third generation wave model for coastal regions: model description and validation. J. Geophys. Res. 104 (C4), 7649–7666.
Box, G.E.P., Jenkins, G., 1976. Time Series Analysis: Forecasting and Control. Holden-Day, San Francisco.
Brekken, T.K.A., Ozkan-Haller, H.T., Simmons, A., 2012. A methodology for large-scale ocean wave power time-series generation. IEEE J. Oceanic Eng. 37, 294–300.
Bunn, D.W., 2004. Modelling Prices in Competitive Electricity Markets. Wiley, New York.
Chawla, A., Spindler, D.M., Tolman, H.L., 2012. Validation of a thirty year wave hindcast using the Climate Forecast System Reanalysis winds. Ocean Model. 70, 189–206.
Deo, M.C., Naidu, C.S., 1998. Real time wave forecasting using neural networks. Ocean Eng. 26, 191–203.
Deo, M.C., Jha, A., Chaphekar, A.S., Ravikant, K., 2001. Neural networks for wave forecasting. Ocean Eng. 28, 889–898.
Deo, M.C., Jagdale, S.S., 2003. Prediction of breaking waves with neural networks. Ocean Eng. 30, 1163–1178.
Durrant, T.H., Woodcock, F., Greenslade, D.J.M., 2008. Consensus forecasts of modeled wave parameters. Weather Forecasting 24, 492–503.
Esteban, M., Leary, D., 2011. Current developments and future prospects of off shore wind and ocean energy. Appl. Energy 90, 128–136.
Garcia-Medina, G., Ozkan-Haller, H.T., Ruggiero, P., Oskamp, J., 2013. An inner-shelf wave forecasting system for the U.S. Pacific Northwest. Weather Forecasting 28, 681–703.
Gaur, S., Deo, M.C., 2008. Real-time wave forecasting using genetic programming. Ocean Eng. 35, 1166–1172.
Granger, C.W.J., 2008. Non-linear models: where do we go next—time varying parameter models? Stud. Nonlinear Dyn. Econometrics 12, Article 1.
Hasselmann, K., Ross, D.B., Müller, P., Sell, W., 1976. A parametric wave prediction model. J. Phys. Oceanogr. 6, 200–228.
Hasselmann, D.E., Dunckel, M., Ewing, J.A., 1980. Directional wave spectra observed during JONSWAP 1973. J. Phys. Oceanogr. 10, 1264–1280.
Hasselmann, S., Hasselmann, K., Allender, J.H., Barnett, T.P., 1985. Computations and parameterizations of the non-linear energy transfer in a gravity wave spectrum. Part II: Parameterizations of the non-linear energy transfer for application in wave models. J. Phys. Oceanogr. 15, 1378–1391.
Henderson, R., 2006. Design, simulation, and testing of a novel hydraulic power take-off system for the Pelamis wave energy converter. Renewable Energy 31, 271–283.
Ho, P.C., Yim, J.Z., 2006. Wave height forecasting by the transfer function model. Ocean Eng. 33, 1230–1248.
Holthuijsen, L.H., 2007. Waves in Oceanic and Coastal Waters. Cambridge University Press.
Jain, P., Deo, M.C., 2007. Real-time wave forecasts off the western Indian coast. Appl. Ocean Res. 29, 72–79.
Janssen, P.A.E.M., 1991. Quasi-linear theory of wind–wave generation applied to wave forecasting. J. Phys. Oceanogr. 21, 1631–1642.
Janssen, P.A.E.M., 2007. Progress in ocean wave forecasting. J. Comput. Phys. 227, 3572–3594.
Kalman, R.E., 1960. A new approach to linear filtering and prediction problems. Trans. Am. Soc. Mech. Eng., J. Basic Eng. 83D, 35–45.
Londhe, S.N., Panchang, V., 2006. One-day wave forecasts based on artificial neural networks. J. Atmos. Oceanic Technol. 23, 1593–1603.
Parkinson, S., Dragoon, K., Reikard, G., Garcia-Medina, G., Ozkan-Haller, H.T., Brekken, T.K.A., 2015. Integrating ocean wave energy at large-scales: a study of the US Pacific Northwest. Renewable Energy 76, 551–559.
Pelamis, 2014. ⟨www.pelamiswave.com⟩.
Pinson, P, Reikard, G, Bidlot, J.R., 2012. Probabilistic forecasting of the wave energy flux. Appl. Energy 93, 364–370.
Reikard, G., 2008. Using temperature and state transitions to forecast wind speed. Wind Energy 11, 431–443. http://dx.doi.org/10.1002/we/263.
Reikard, G., 2009. Predicting solar radiation at high resolutions: a comparison of time series forecasts. Solar Energy 83, 342–349. http://dx.doi.org/10.1016/j.solener.2008.08.07.
Reikard, G., 2010. Regime-switching models and multiple causal factors in forecasting wind speed. Wind Energy 13, 407–418. http://dx.doi.org/10.1002/we.361.
Reikard, G., Pinson, P., Bidlot, J.R., 2011. Forecasting Ocean Wave Energy: the ECMWF wave model and time series methods. Ocean Eng. 38, 1089–1099.
Reikard, G., 2013. Integrating wave energy into the power grid: simulation and Forecasting. Ocean Eng. 73, 168–178.
Retzler, C., 2006. Measurements of the slow drift dynamics of a model Pelamis wave energy converter. Renewable Energy 31, 257–269.
Robertson, B., Hiles, C., Buckham, B., 2014. Characterizing the nearshore energy resources on the west coast of Vancouver Island. Renewable Energy 71, 665–678.
Roulston, M.S., Ellepola, J., von Hardenberg, J., Smith, L.A., 2005. Forecasting wave height probabilities with numerical weather prediction models. Ocean Eng. 32, 1841–1863.
Rossi, B., Inoue, A., 2012. Out-of-sample forecast tests robust to the choice of window size. J. Bus. Econ. Stat. 30, 432–453.
SWAN, 2006. SWAN Cycle III, Version 40.51. ⟨http://falk.ucsd.edu/modeling/swanuse.pdf⟩.
Tsai, C.P., Lin, C., Shen, J.N., 2002. Neural network for wave forecasting among multi-stations. Ocean Eng. 29, 1683–1695.
Tseng, C.M., Jan, C.D., Wang, J.S., Wang, C.M., 2007. Application of artificial neural networks in typhoon surge forecasting. Ocean Eng. 34, 1757–1768.
Wavestar, 2014. ⟨www.wavestarenergy.com⟩.
Wittmann, P.A., 2001. Implementation of WaveWatch III at fleet numerical meteorology and oceanography center. In: IEEE Oceans Conference. 3, 1474–1479.
Woodcock, F., Engel, C., 2005. Operational consensus forecasts. Weather Forecasting 20, 101–111.
Woodcock, F, Greenslade, D.J.M., 2006. Consensus of numerical forecasts of significant wave heights. Weather Forecasting 22, 792–803.
Yemm, R., Pizer, D., Retzler, C., Henderson, R., 2012. Pelamis: experience from concept to connection. Philos. Trans. R. Soc. 370, 365–380.
Zamani, A., Solomatine, D., Azimian, A., Heemink, A., 2008. Learning from data for wind–wave forecasting. Ocean Eng. 35, 953–962.